Local baroclinic instability of flow over variable topography

By R. M. SAMELSON AND J. PEDLOSKY

Woods Hole Oceanographic Institution, Woods Hole, MA 02543, USA

Local baroclinic instability is studied in a two-layer quasi-geostrophic model. Variable meridional bottom slope controls the local supercriticality of a uniform zonal flow. Solutions are found by matching pressure, velocity, and upper-layer vorticity across longitudes where the bottom slope changes abruptly so as to destabilize the flow in a central interval of limited zonal extent. In contrast to previous results from heuristic models, an infinite number of modes exist for arbitrarily short intervals. For long intervals, modal growth rates and frequencies approach the numerical and WKB results for the most unstable mode. For intervals of length comparable to and smaller than the wavelengths of unstable waves in the homogeneous problem, the WKB results lose accuracy. The modes retain large growth rates (about half maximum) for intervals as short as the internal deformation radius. Evidently, the deformation radius and not the homogeneous instability determines the fundamental scale for local instability. Maximum amplitudes occur near the downstream edge of the unstable interval. Lower-layer amplitudes decay downstream more rapidly than upper-layer amplitudes. For short intervals, the instability couples motions with widely disparate horizontal scales in the upper and lower layers. Heat flux is more strictly confined than amplitude. Growth rates increase linearly with weak supercriticality.

1. Introduction

Cyclone scale disturbances in mid-latitude atmospheric flow arise owing to the baroclinic instability of the westerly winds found in mid-latitudes. Since the pioneering work of Charney (1947) and Eady (1949) a continuing development of the original analysis has sought to bring the early idealized models into closer correspondence with the complex nature of the observed atmospheric flow. An especially common idealization, used for technical simplicity, has been to represent the basic flow as independent of longitude (the downstream direction). In the classical problems cited above, the zonal flow was a function only of height. Observations (e.g. Holopainen 1983) emphasize the presence of regions of intensified shear in the mean winds along the major storm track off the eastern coasts of the American and Asian continents. The frequency of cyclone development is strongly enhanced in these regions. It seems clear that understanding the geographical distribution and structure of the disturbances requires a consideration of currents whose stability properties vary in the downstream direction.

Previous attempts to treat zonally-varying flows (Gent & Leach 1976; Merkine & Shafranek 1980; Pierrehumbert 1984) have relied heavily on the assumption that the basic flow variations occur on a scale large relative to the disturbance wavelengths, so that WKB (Liouville–Green) techniques may be used. These studies have revealed
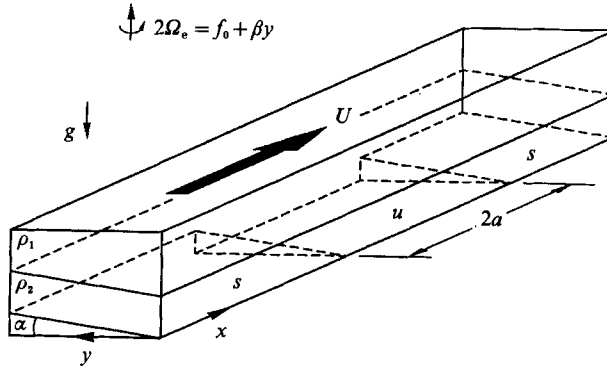
FIGURE 1. The two-layer model. The basic zonal flow U is in the upper layer. The bottom slope is non-zero for $|x| > a$ and locally stabilizes the flow outside the region $|x| < a$. The region marked u is locally unstable while the marked s is locally stable.

the existence under certain conditions of local instabilities associated with relative maxima in the baroclinicity. The unstable modes are local or 'trapped' in that they grow in time but decay in space away from a point downstream of the baroclinicity maximum. This approach, though fruitful, has been limited by the assumption that the basic state variations have much larger scale than the disturbance wavelength. In particular, when the downstream length of the interval of locally unstable flow is the same order as the characteristic wavelength of the instability, important questions arise as to the number, structure and growth rate of unstable modes (should any persist as the interval shrinks). These questions, by their very nature, are not appropriately dealt with by the WKB technique. Numerical methods (e.g. Frederiksen 1983) can circumvent the limitations and idealizations of the WKB approximation, but the complexity of the results and the limitations imposed by computing capacity produce complementary difficulties in understanding the basic processes involved in zonally varying unstable flow instabilities.

In the present paper we pursue an alternative path. We focus on the downstream variation of the *supercriticality* of the basic flow rather than on the variation of the flow's baroclinicity or shear. We consider a two-layer β-plane model of atmospheric flow in which, in the absence of disturbances, the flow is limited to the upper layer and independent of cross-stream and downstream coordinates. Were the bottom relief simply flat, the problem would reduce to the classical Phillips problem (Phillips 1954). As is well known, instability in that model requires that a westerly shear exceed a critical value for which the potential vorticity gradient of the lower layer changes sign. In this study we add a meridional bottom slope in the lower layer, which enhances the β-effect and renders the flow stable except in a central region of limited zonal extent, where the slope is absent and the flow may be locally unstable (see figure 1). This case is of natural physical interest, given the influence of topography on many atmospheric and oceanic flows. The technical advantage of this way of yielding downstream variation of the supercriticality is that a forced wave is not required (since the basic zonal flow is taken to be zero at the lower boundary) and, more important, it is consistent to consider the basic state as a truly parallel flow. This avoids the confusion between the effects of downstream variations in supercriticality and the effects of curvature in the basic flow streamlines. The latter would inevitably occur were we to consider a flow whose baroclinicity varied downstream. The zonal convergence of the flow would force a meridional velocity

which would become important precisely in the parameter region of interest, i.e. when the scale of downstream variation of supercriticality is of the same order as the scale of the instability.

Since the basic flow is independent of the zonal coordinate in each subregion of the flow, solutions may be found by elementary methods. Matching constant-slope solutions across the edges of the central interval (where the slope changes abruptly) yields an eigenvalue problem for the unstable modes that is analogous to the potential well problems of quantum mechanics. This approach was originally proposed for the baroclinic instability problem by Pedlosky (1989), who restricted attention to a pair of heuristically-derived model equations. Here, we pursue this investigation with a quasi-geostrophic model.

2. Formulation

The model we will use is the two-layer, quasi-geostrophic model and requires that the timescale of the motion be long enough for the primary momentum balance to be geostrophic. Each layer has a uniform density and the horizontal velocities are independent of depth within each layer. The layers have equal mean depth. The governing equations are the quasi-geostrophic potential vorticity equations. The reader is referred to Pedlosky (1979) for a complete derivation.

The equations in non-dimensional form are

$$\frac{\partial Q_1}{\partial t} + J(\psi_1, Q_1) = 0, \qquad (1a)$$

$$\frac{\partial Q_2}{\partial t} + J(\psi_2, Q_2) = -r\nabla^2\psi_2. \qquad (1b)$$

Here ψ_j is the streamfunction in layer $j, j = 1,2$ where 1 refers to the upper layer and Q_j is the corresponding potential vorticity

$$Q_1 = \nabla^2\psi_1 - (\psi_1 - \psi_2) + \beta y, \qquad (2a)$$

$$Q_2 = \nabla^2\psi_2 - (\psi_2 - \psi_1) + \beta y + h(x,y). \qquad (2b)$$

The terms $\nabla^2\psi_j$ represent the relative vorticity while the terms $\psi_1 - \psi_2$ are the scaled interface displacements and represent vortex stretching. The Cartesian coordinates x and y are positive eastward and northward, respectively. The Jacobian J is defined as

$$J(a,b) = \frac{\partial a}{\partial x}\frac{\partial b}{\partial y} - \frac{\partial a}{\partial y}\frac{\partial b}{\partial x}. \qquad (3)$$

Horizontal distance has been non-dimensionalized by the internal radius of deformation $L_R = (g'D)^{\frac{1}{2}}/f_0$ (the scale of developing instabilities in the zonally uniform problem, which have wavelengths about $2\pi L_R$), and the rigid-lid approximation has been made. D is the depth of each layer, and f_0 is the value of the Coriolis parameter at the central latitude on the β-plane. Velocities are scaled by U_*, the magnitude of the upper-layer mean flow, which is taken to be uniform. Time is scaled by the adjective time L_R/U_*. A parameter of particular importance is $\beta = \beta_* L_R^2/U_*$, where β_* is the (dimensional) northward gradient of the Coriolis parameter. The non-dimensional parameter β measures the relative size of the potential vorticity gradient due to the earth's sphericity compared to the potential

vorticity gradient associated with the vertical shear of the zonal current. For zonally uniform vertical shear U_*, β must be less than 1 for instability (in the absence of topographic relief). The friction coefficient r is the ratio of the adjective timescale divided by the spin-up time due to Ekman-layer friction.

The presence of bottom topography will contribute to the potential vorticity of the lower layer. If h_* is the dimensional amplitude of the bottom relief, this additional potential vorticity is represented by the term $h(x,y)$ in (2b) where

$$h(x,y) = \frac{h_*}{D}\frac{L_R f_0}{U_*}. \tag{4a}$$

Since the quasi-geostrophic approximation requires $U_*/L_R f_0 \ll 1$, this means that $h_* \ll D$ is required so that h be of order one. We consider topography of the form

$$h = y\alpha(x), \tag{4b}$$

where the x-dependent slope α will be such as to stabilize flow for all $|x| > a$. Since the bottom depth varies zonally the basic state must have no flow in the lower layer. The model geometry is illustrated in figure 1.

For simplicity, and because the gravest meridional mode is typically the most unstable one, we restrict our attention to disturbances which are independent of the meridional coordinate. This is a consistent local approximation to a flow that is nearly uniform meridionally in a sufficiently large region (as in the centre of a meridionally-bounded zonal channel such as is often used to represent the mid-latitude atmosphere). Since the perturbation velocities are then only in the y-direction, no flow in the lower layer traverses the sharp changes in the bottom topography in the x-direction.

The streamfunctions for the flow may be written

$$\psi_1 = -Uy + \phi_1(x,t), \tag{5a}$$

$$\psi_2 = \phi_2(x,t). \tag{5b}$$

where $\phi_j(x,t)$ represents the perturbation streamfunction in the jth layer. (U has been scaled out of the problem, except for a choice of sign, by the choice of velocity scale U_*. It is convenient to take U_* positive, so that β remains positive for westward flow. In the following, we consider only $U = 1$ or $U = -1$.)

The linearized problem for the evolution of the disturbances now follows from (1), (2) and (5) as,

$$q_{1t} + Uq_{1x} + (\beta+U)\phi_{1x} = 0, \tag{6a}$$

$$q_{2t} + (\beta_2-U)\phi_{2x} = -r\phi_{2xx}, \tag{6b}$$

where

$$q_j = \phi_{jxx} + (-1)^j(\phi_1-\phi_2) \quad (j=1,2), \tag{7}$$

$$\beta_2 = \beta + \alpha(x). \tag{8}$$

It is clear from (6)–(8) that the disturbances will remain independent of y if they are so initially. Since only horizontal derivatives (and not the local value) of the barotropic streamfunction $\phi_B = \phi_1 + \phi_2$ enter the potential vorticity balance, it is convenient to rewrite (6) and (7) in terms of the barotropic velocity v_B and the thermal streamfunction ϕ_T, where

$$v_B = \phi_{1x} + \phi_{2x}, \tag{9a}$$

$$q_T = \phi_1 - \phi_2, \tag{9b}$$

In these variables, (6) and (7) become

$$q_{Bt} + \tfrac{1}{2}U(q_{Bx} + q_{Tx}) + \beta v_B + U\phi_{Tx} + \tfrac{1}{2}\alpha(x)(v_B - \phi_{Tx}) = -\tfrac{1}{2}r(v_{Bx} - \phi_{Txx}), \quad (10a)$$

$$q_{Tt} + \tfrac{1}{2}U(q_{Bx} + q_{Tx}) + \beta\phi_{Tx} + Uv_B - \tfrac{1}{2}\alpha(x)(v_B - \phi_{Tx}) = \tfrac{1}{2}r(v_{Bx} - \phi_{Txx}), \quad (10b)$$

where
$$q_B = v_{Bx}, \quad (10c)$$

$$q_T = \phi_{Txx} - 2\phi_T. \quad (10d)$$

We consider only local instability, and so require the disturbances to decay for large $|x|$,

$$v_B, \phi_T \to 0 \quad \text{as } x \to \pm\infty. \quad (11)$$

The simplified problem (10)–(11) retains the essential physics of the local instability, while filtering out the effects of meridional confinement. Further, the perturbation velocities are purely meridional, so that the local meridional topographic slope enters the vorticity balance (10) but the zonal slope does not.

After the solution of (10)–(11) has been obtained in terms of v_B and ϕ_T, the streamfunctions ϕ_1 and ϕ_2 may be computed by integrating (9a) over x,

$$\phi_1 = \frac{1}{2}\left(\int_\infty^x v_B \, \mathrm{d}x' + \phi_T\right), \quad (12a)$$

$$\phi_2 = \frac{1}{2}\left(\int_\infty^x v_B \, \mathrm{d}x' + \phi_T\right). \quad (12b)$$

Note that the barotropic streamfunction

$$\phi_B = \int_\infty^x v_B \, \mathrm{d}x'$$

need not vanish as $x \to -\infty$, though v_B must by (11). Physically, this is because long barotropic waves propagate westward arbitrarily fast for arbitrarily small meridional wavenumber, so that a barotropic disturbance 'at infinity' (the limit $x \to -\infty$) must be allowed in the meridionally uniform case we consider. (The westward propagation determines the constant of integration (12).) Integrating (10a) over x and using (9) and (11) yields

$$\int_{-\infty}^\infty \alpha\phi_{2x} \, \mathrm{d}x + \beta\int_{-\infty}^\infty v_B \, \mathrm{d}x = 0, \quad (13)$$

an integral statement of potential vorticity conservation for meridional motion in the ambient (topographic and planetary) potential vorticity gradients. Note that (13) is a potential vorticity balance and not a statement of mass conservation, which is itself guaranteed in the quasi-geostrophic approximation by the streamfunction representation of the flow field and the restriction to small-amplitude topography. The net barotropic meridional flow in the planetary potential vorticity gradient is diagnostically related by (13) to the net lower-layer meridional flow in the topographic potential vorticity gradient.

Before proceeding with the instability problem, it is useful to review the plane wave solutions of (10) for constant bottom slope α, and their stability properties. These are of the form

$$v_B = A_B \, \mathrm{e}^{\mathrm{i}(kx - \omega t)}, \quad \phi_T = A_T \, \mathrm{e}^{\mathrm{i}(kx - \omega t)}, \quad (14)$$
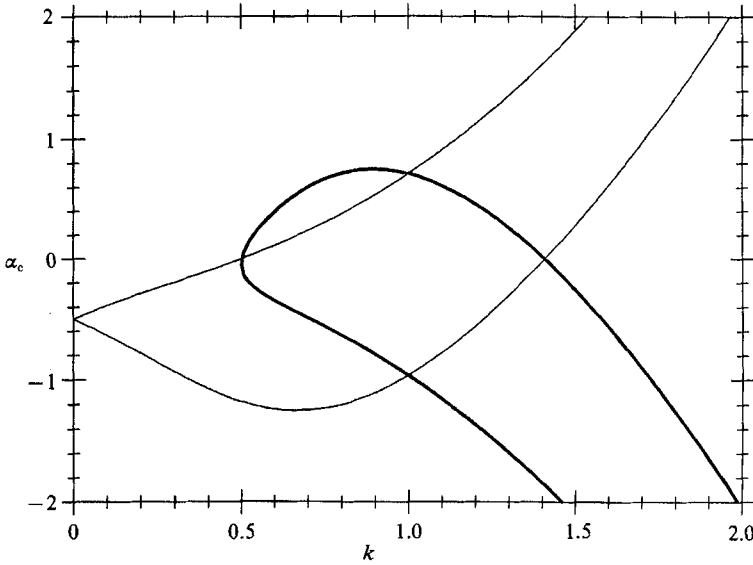
FIGURE 2. Critical slope α_c versus wavenumber k for plane waves over constant slope, $r = 0$, $\beta = 0.25$. ———, $U = 1$; ———, $U = -1$.

where k and ω are in general complex and satisfy the dispersion relation

$$G(\omega, k) = 0, \tag{15a}$$

where
$$G(\omega, k) = k(k^2 + 2)\,\omega^2 + [-Uk^2(k^2 + 2) + (\beta + \beta_2 + irk)\,(k^2 + 1)]\,\omega$$

$$+ (\beta_2 - U + irk)\,(\beta - Uk^2)\,k. \tag{15b}$$

(These plane waves do not, of course, satisfy (11).) The complex amplitudes A_B and A_T satisfy

$$[(\omega - kU)\,k + (\beta + U)]\,A_B + i\,[(\omega - kU)\,(k^2 + 2) + (\beta + U)\,k]\,A_T = 0. \tag{16}$$

Equations (6) have the additional degenerate solution $k = 0$, $\phi_1 = \phi_2$, ω arbitrary, for which $v_B = \phi_T = 0$ identically. The allowed barotropic disturbance 'at infinity' (see above) has this character locally. The critical slope α_c for instability of the plane waves may be obtained from (15), regarded as a quadratic polynomial in ω, by setting the discriminant equal to zero, which in turn yields a quadratic in α_c. The result is shown in figure 2 for $r = 0$, $\beta = 0.25$, and $U = \{-1, 1\}$. (The value of β was chosen for comparison with Pierrehumbert 1984.) Inside the tongue-shaped critical curves, waves are unstable. Outside, they are stable. Thus for $U = 1$, there is stability for $\alpha > U - \beta = 0.75$ for all wavenumbers, while there is a band of unstable waves for $\alpha < 0.75$. For $U = -1$, the inequalities are reversed, with stability for $\alpha < U - \beta = -1.25$ and a band of instability for $\alpha > -1.25$.

We now proceed with the local instability problem. For various bottom-slope configurations $\alpha(x)$, chosen such that the flow satisfies the plane wave criterion for instability in a central region of limited zonal extent, we obtain unstable eigenmodes of (10)–(11) in three ways. Our primary approach is a matching technique. We consider a situation in which the bottom slope has a constant value $\alpha = \alpha_u$ in the interior region $|x| < a$ and a different constant value $\alpha = \alpha_s$ in the exterior region

$|x| > a$. Values of α_u and α_s are considered such that plane waves are unstable for $\alpha = \alpha_u$ and stable for $\alpha = \alpha_s$ (see figures 1 and 2). For given α and ω, the dispersion relation (15) may be solved for its four roots $k_j, j = 1, \ldots, 4$. In each of the three regions $x < -a$, $|x| < a$, and $x > a$, solutions are sought in the form of linear combinations of these four waves,

$$v_{\mathrm{B}} = \sum_{j=1}^{4} A_{\mathrm{B}j} \mathrm{e}^{\mathrm{i}(k_j x - \omega t)}, \quad \phi_{\mathrm{T}} = \sum_{j=1}^{4} A_{\mathrm{T}j} \mathrm{e}^{\mathrm{i}(k_j x - \omega t)}. \tag{17}$$

The coefficients $A_{\mathrm{B}j}$ and $A_{\mathrm{T}j}$ will differ in different regions, but we make this dependence implicit for notational convenience.

The boundary conditions (11) require that the modes decay for $|x| \gg a$, so only waves with imaginary part of k_j negative can contribute for $x < -a$, and waves with imaginary part of k_j positive for $x > a$. These conditions must be supplemented by matching ('jump') conditions at the points $x = \pm a$. Four of these are continuity of pressure,

$$\phi_1, \phi_2 \text{ continuous at } x = \pm a. \tag{18}$$

The other six are obtained from the dynamical equations by a method that is standard for problems of this type: the equations (6) are integrated across regions of width ϵ around $x = a$ or $x = -a$ in which the rapid variation in slope is smooth, and then ϵ is allowed to approach zero under the condition that (18) hold. The result is that meridional velocity and upper-layer vorticity must also be continuous,

$$\phi_{1x}, \phi_{2x}, \phi_{1xx} \text{ continuous at } x = \pm a. \tag{19}$$

There is no mean flow advection of perturbation vorticity in the lower layer, so the lower-layer equation (6b) is of reduced order in x and continuity of ϕ_{2xx} at $x = \pm a$ is not required. Since the barotropic streamfunction is obtained by the integration (12), it is sufficient to require the eight matching conditions

$$\phi_{\mathrm{T}}, v_{\mathrm{B}}, \phi_{\mathrm{T}x}, v_{\mathrm{B}x} + \phi_{\mathrm{T}xx} \text{ continuous at } x = \pm a. \tag{20}$$

Alternatively, these may be obtained directly from (10) and (18) by the above procedure.

Applying (11) and (20) to the linear combinations (17) of plane wave solutions in the interior and exterior regions yields a nonlinear 8×8 matrix eigenvalue problem for the complex frequency $\omega = \omega_r + \mathrm{i}\omega_i$ and the coefficients $A_{\mathrm{B}j}, A_{\mathrm{T}j}$ in each region. The spatial structure of the modes is represented by $\hat{v}_{\mathrm{B}}$ and $\hat{\phi}_{\mathrm{T}}$, where

$$\hat{v}_{\mathrm{B}}(x) = \sum_{j=1}^{4} A_{\mathrm{B}j} \mathrm{e}^{\mathrm{i}k_j x}, \tag{21}$$

$$\hat{\phi}_{\mathrm{T}}(x) = \sum_{j=1}^{4} A_{\mathrm{T}j} \mathrm{e}^{\mathrm{i}k_j x}, \tag{22}$$

and the coefficients $A_{\mathrm{B}j}$ and $A_{\mathrm{T}j}$ may (will) be different in each of the three regions. The eigenmodes are then

$$v_{\mathrm{B}} = \mathrm{Re}\{\hat{v}_{\mathrm{B}} \mathrm{e}^{-\mathrm{i}\omega t}\}, \quad \phi_{\mathrm{T}} = \mathrm{Re}\{\hat{\phi}_{\mathrm{T}} \mathrm{e}^{-\mathrm{i}\omega t}\}, \tag{23}$$

where now (21) and (22) may be multiplied by a single complex number to give a particular initial amplitude and phase of the disturbance. The eigenvalue problem is solved numerically by finding zeros of the determinant, which is efficiently done using Gaussian elimination to simplify the evaluation of the determinant at each

iteration. For small ω, a perturbation theory is also given, which yields a more detailed physical picture of the mode structure and a check on the numerics.

In summary, the matching technique yields solutions (unstable eigenmodes) of the local instability problem in which the meridional slope α has abrupt zonal variations. These solutions depend on the half-length a of the unstable interval as well as on the parameters U, β, and r and the slopes α_s and α_u. The frequencies and growth rates ω_r and ω_i of these modes are the real and imaginary parts, respectively, of the eigenvalues ω. These are the special values of ω for which the linear combinations (17) of locally-plane waves can satisfy the boundary and matching conditions (11) and (20) to form eigenmodes. A similar approach in quantum mechanics leads to quantization of modes in a potential well, as only half-integral wavelengths can satisfy the appropriate boundary conditions. Quantization of modes can be anticipated by analogy here as well, although the physics is obviously quite different.

We supplement the matching approach with two other methods that yield the most unstable mode for smoothly varying slope α. Our second method is to numerically timestep (10) from random or Gaussian wave-packet initial conditions until the most unstable mode emerges. We use a leapfrog marching scheme with 512 Fourier modes and a non-aliasing spectral transform method to efficiently evaluate the topographic term $\alpha(x)[v_B(x, t) - \phi_{Tx}(x, t)]$. The horizontally averaged barotropic velocity is obtained from (13) at each timestep. Growth rate and frequency are determined from total perturbation kinetic energy and zero crossings of the perturbation streamfunction, respectively. Finally, we use WKB techniques to analyse the timestepping solutions, following Pierrehumbert (1984).

3. Matching solutions

We have used the matching technique described above to find unstable eigenmodes as a function of the interval half-length a of the interval of instability $|x| < a$, holding other parameters fixed. We discuss results for both eastward and westward basic state velocity U. In this and the next section, we consider only inviscid instabilities ($r = 0$), deferring a discussion of frictional effects to §5.

Consider a uniform eastward upper-flow $U = 1$ over a flat bottom ($\alpha = 0$) with $\beta = 0.25$. According to figure 2, this homogeneous flow will be unstable to perturbations with wavenumbers $k \approx 1$. Suppose instead that the bottom slopes up northward uniformly, with $\alpha = 2$. This changes the sign of the potential vorticity gradient in the lower layer, and stabilizes the flow (figure 2). We now examine the local instability problem in which the bottom is flat in the interval of instability ($\alpha = \alpha_u = 0$ for $|x| < a$) and slopes up northward to stabilize the flow outside this interval ($\alpha = \alpha_s = 2$ for $|x| > a$).

Figure 3 shows the eigenvalues $\omega = \omega_r + i\omega_i$ obtained for the first three modes for $U = 1$, $\beta = 0.25$, $\alpha_u = 0$, $\alpha_s = 2$, as a function of interval half-length a. The modes are ordered by decreasing growth rate ω_i, so that the first mode is the most unstable. All three modes have eigenvalues with positive imaginary parts, and so, by (23), are indeed unstable modes that grow exponentially with time. The growth rates (and frequencies) of all three modes decrease monotonically as the interval half-length a decreases to zero. For large a, the values approach the WKB results for slowly varying slope, whose derivation will be discussed below. For small a, the basic state approaches the homogeneous case with uniform stabilizing slope, and the growth rates vanish when a reaches zero. Remarkably, all three modes have non-zero growth rates for arbitrarily small a. This is in marked contrast to the model problems of
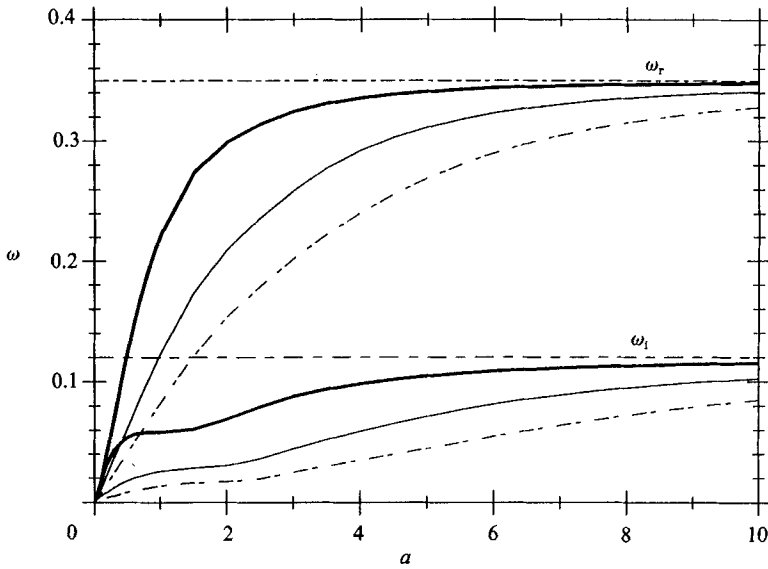
FIGURE 3. Frequency ω_r and growth rate ω_i versus interval half-length a for local instability eigenmodes $U = 1$, $\beta = 0.25$, $\alpha_u = 0$, $\alpha_s = 2$. ——, Mode 1; ——, mode 2; —·—, mode 3; horizontal ———, WKB result.

Pedlosky (1989), in which the growth rates of successively higher modes first become non-zero at successively longer intervals of instability. A perturbation theory given below indicates that an infinite number of unstable modes exist for arbitrarily small a.

There are two regions of relatively rapid change in growth rate in figure 3. The model growth rates and frequencies first begin to deviate significantly from the WKB values near $a = 3$, where the interval length $2a$ roughly equals the wavelengths of the homogeneous unstable waves. (From figure 2, the unstable waves in the homogeneous case have wavenumbers $k \approx 1$ and wavelengths $\lambda \approx 2\pi$.) Substantial growth rates are maintained even for interval lengths an order of magnitude smaller than those wavelengths. For $a = 0.5$, where the interval length equals the deformation radius, the growth rate for mode 1 is still roughly half its maximum value. In comparison, the shortest unstable wave in the homogeneous flat-bottom flow has a wavelength greater than four deformation radii. This is an unexpected result: an interval of instability that is short relative to the wavelengths of the instabilities in the homogeneous problem can support rapidly growing modes. For smaller intervals, the growth rate rapidly decreases. Evidently, the fundamental cutoff scale for the instability is the deformation radius, not the wavelengths of the homogeneous instabilities.

The spatial structure of the modes changes with the interval length, becoming increasingly depth-dependent as the length decreases. Figure 4(a) shows velocities in layers 1 and 2 for mode 1 for $a = 10$, an interval of instability 20 deformation radii in extent. The solid lines are $v_1 = \phi_{1x}$ and $v_2 = \phi_{2x}$ (from (12) and (23) at $t = 0$), while the dashed lines are $|\hat{v}_1|$ and $-|\hat{v}_2|$, where $\hat{v}_1$ and $\hat{v}_2$ represent the spatial structure of the eigenmodes (from (21) and (22)). The disturbances attain maximum amplitude near the 'exit point', the downstream edge of the interval of instability. Here 'downstream' is meant with respect to both the upper-layer velocity U and the phase and group velocities of the unstable waves in the homogeneous case, which can be
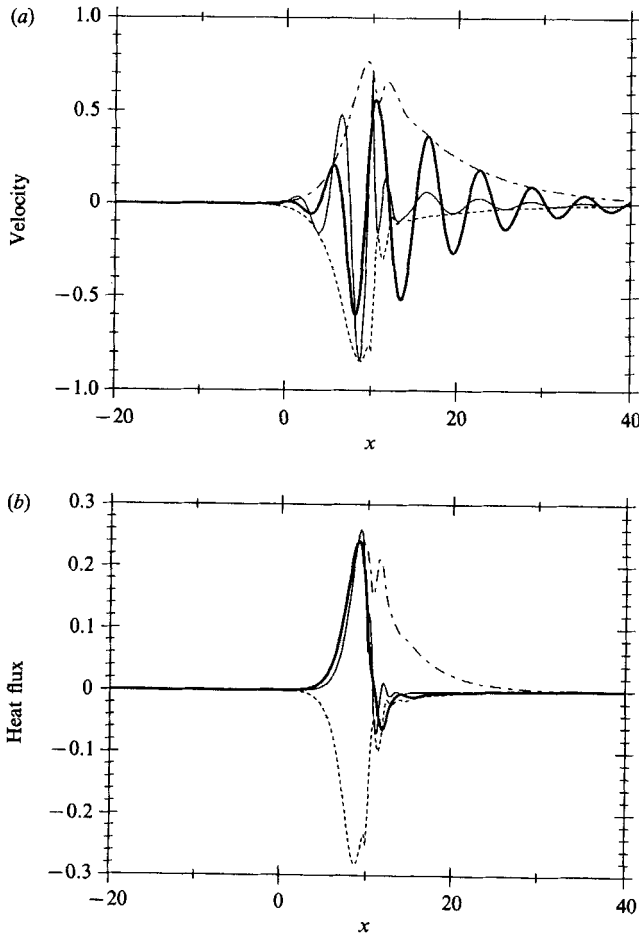
FIGURE 4 (a, b). For caption see page 422.

shown to be co-directional for basic flows over a flat bottom with zero lower-layer velocity. Physical reasoning and the model problem of Pedlosky (1989) suggest that the sign of the group velocity (the velocity at which energy propagates) should in general determine the location of the exit point. In the interval of instability, the disturbance grows downstream rapidly enough that it is negligible in the upstream third and small in the middle third, relative to the downstream third. This downstream intensification in the interval, with disturbance maximum near the exit point, was observed in the model problems of Pedlosky (1989) and by Pierrehumbert (1984). Downstream of the exit point, the modes decay in space (while growing in time). In the interval, upper- and lower-layer velocities are nearly equal in magnitude (compare $|\hat{v}_1|$ and $|\hat{v}_2|$ in figure $4a$). Downstream of the exit point, the velocity is much larger in the upper layer, as the lower-layer disturbance (which is in direct contact with the stabilizing bottom slope) decays rapidly near the exit point. Crest-to-crest wavelengths for the oscillations in the amplitude envelope are of order 2π, comparable to the wavelengths of the unstable homogeneous waves. The downstream decay scale in the upper layer is also comparable to these wavelengths.

The phase shift with height characteristic of baroclinic instabilities is westward in the unstable interval in figure $4(a)$, as it must be for northward heat flux. Outside the
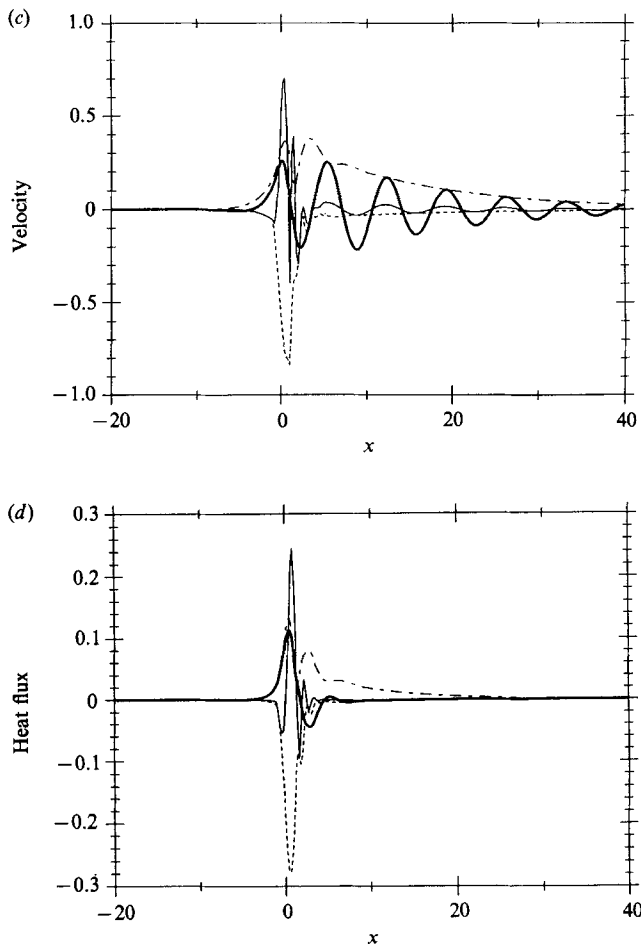
FIGURE 4 (*c, d*). For caption see next page.

interval, the phase shift decays rapidly to zero, so the heat flux will be confined near the unstable interval. Heat flux in the two-layer model is represented by advection of the interface height $\eta = \phi_T = \phi_1 - \phi_2$. The zonally integrated heat flux is equal in the two layers, since $\eta \to 0$ as $x \to \pm \infty$:

$$\int_{-\infty}^{\infty} v_1 \phi_T \, dx = \int_{-\infty}^{\infty} \phi_{1x} \phi_T \, dx$$

$$= \int_{-\infty}^{\infty} \phi_{2x} \phi_T \, dx + \int_{-\infty}^{\infty} \phi_{Tx} \phi_T \, dx$$

$$= \int_{-\infty}^{\infty} v_2 \phi_T \, dx, \tag{24}$$

where $v_1 = \phi_{1x}$ and $v_2 = \phi_{2x}$ are the meridional velocities in layers 1 and 2, respectively.

The heat flux in layer j may be written

$$v_j \phi_T = \tfrac{1}{2} \text{Re} \, (\hat{v}_j \, \hat{\phi}_T^*) \, e^{2\omega_i t} + \tfrac{1}{2} \text{Re} \, (\hat{v}_j \, \hat{\phi}_T \, e^{-2i\omega_r t}) \, e^{2\omega_i t}, \tag{25}$$
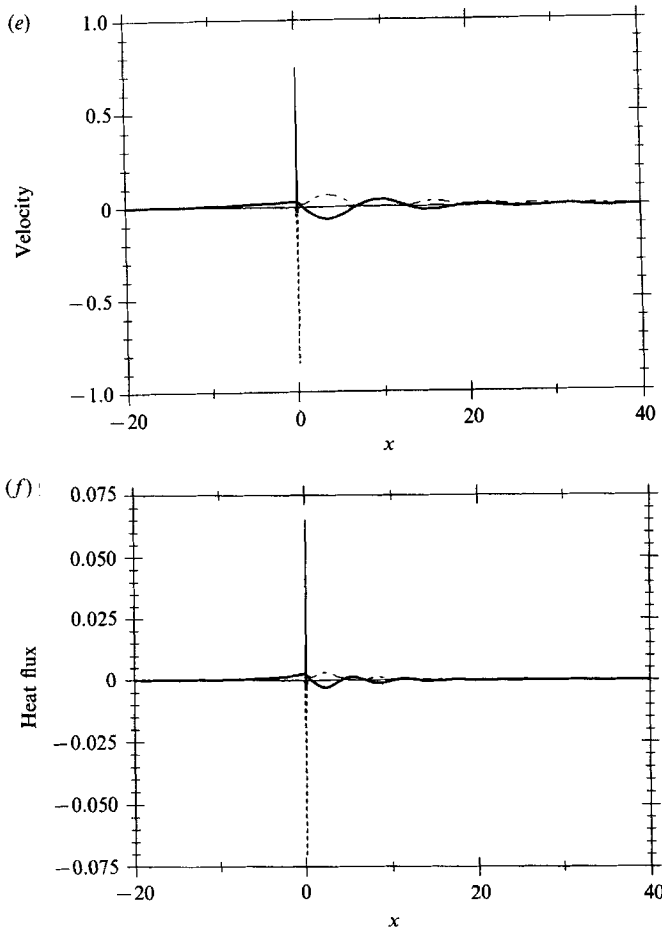
FIGURE 4. Layer velocities and heat fluxes versus x for mode 1, $U = 1$, $\alpha_u = 0$, $\alpha_s = 2$. (a), (c), (e) ——, v_1; ——, v_2; ---, $|\hat{v}_1|$; ---, $-|\hat{v}_2|$. (b), (d), (f) ——, $\frac{1}{2}\mathrm{Re}(\hat{v}_2\,\hat{\phi}_\mathrm{T}^*)$; —— $\frac{1}{2}\mathrm{Re}(\hat{v}_2\,\hat{\phi}_\mathrm{T}^*)$; ---, $\frac{1}{2}|\hat{v}_1\,\hat{\phi}_\mathrm{T}|$; ---, $-\frac{1}{2}|\hat{v}_2\,\hat{\phi}_\mathrm{T}|$. (a), (b) $a = 10$, (c), (d) $a = 1.0$, (e), (f) $a = 0.1$.

where asterisk means complex conjugate. The phase-dependent (second) term does not vanish on averaging over an oscillation period $2\pi/\omega_\mathrm{r}$ because of the exponential growth, but it may be removed by ensemble-averaging over phase or normalizing by the growth before averaging over the oscillation period. The remaining first term may be called the 'phase-averaged' heat flux.

Figure 4 (b) shows the phase-averaged heat flux $\frac{1}{2}\mathrm{Re}(\hat{v}_j\,\hat{\phi}_\mathrm{T}^*)$ (solid lines) and the amplitude $\frac{1}{2}|\hat{v}_j\,\hat{\phi}_\mathrm{T}|$ of the phase-dependent heat flux in each layer for the mode of figure 4 (a). The phase-averaged heat fluxes are nearly identical in the two layers, and are confined to a narrow region near the exit point. The phase-dependent heat flux has an oscillatory structure, with wavelength and downstream decay scale roughly half those of the velocities. As is the case for the velocities, the downstream decay of the phase-dependent heat flux is much more rapid in the lower layer than in the upper.

Figures 4 (c) and 4 (d) show the velocities and heat fluxes for mode 1 for $a = 1$, an interval of instability $2L_\mathrm{R}$ in length. In and near the interval, the horizontal scale of the disturbance is now much smaller in the lower layer than in the upper, where it is nearly unchanged. Peak lower-layer velocities are twice peak upper-layer velocities.
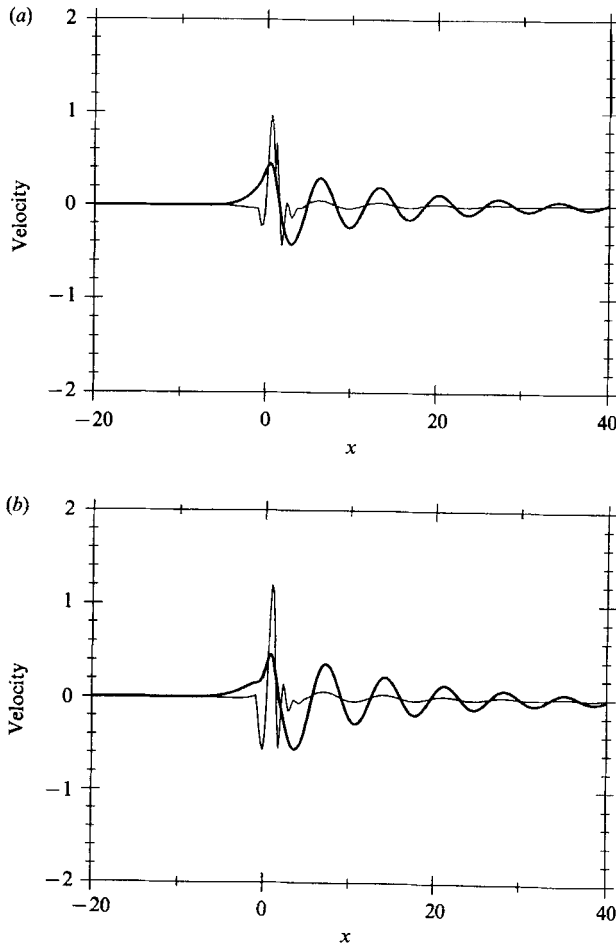
FIGURE 5 (a, b). For caption see next page.

The vertical structure of the heat flux is similar, with shorter horizontal scales and larger peak values in the lower layer. The peak values tend to be at the exit point, though for upper-layer velocity the peak is several deformation radii downstream.

Figure 5 $(a\text{--}d)$ shows mode 1 for $a = 1$ for $t = \pi/(4\omega_r), \pi/(2\omega_r), 3\pi/(4\omega_r), \pi/\omega_r$, for the initial amplitude and phase as in figure 4 (c). The evolution of the spatial structure is complex, as it includes both phase propagation and growth. Note that at any fixed point, the observed signal will be a simple growing oscillation proportional to $\exp(-i\omega t)$. Thus at $t = \pi/\omega_r$, the velocities are equal to $-\exp(\omega_i \pi/\omega_r)$ times their values at $t = 0$.

Figures 4 (e) and 4 (f) show the velocities and heat fluxes for mode 1 for $a = 0.1$, an interval of instability $0.2L_R$ in length. This short interval is roughly one-thirtieth the wavelength of an unstable wave in the homogeneous case, and less than one-twentieth the wavelength of the shortest such unstable wave. The evolution in the lower layer toward short horizontal scale with short interval length has proceeded to an extreme, with the lower-layer disturbance confined to a narrow jet with velocity maximum at the exit point. The jet fluctuates in direction (and grows) with time. The upper-layer disturbance is dominated by a quasi-stationary Rossby wave (wavenumber $k \approx (\beta/U)^{\frac{1}{2}}$) that decays downstream and has negligible lower-layer
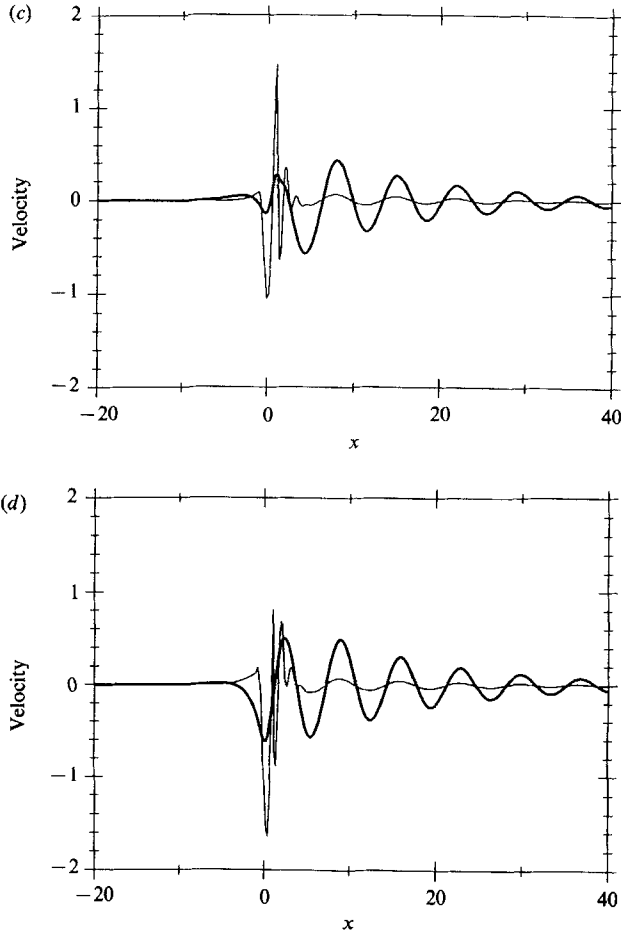
FIGURE 5. Layer velocities ——, v_1 and ——, v_2 for mode 1 from figure 3(c) at (a) $t = \pi/(4\omega_r)$, (b) $t = \pi/(2\omega_r)$, (c) $t = 3\pi/(4\omega_r)$, (d) $t = \pi/\omega_r$.

amplitude. The heat fluxes have similar structure, with the wavelength of the upper-layer flux half that of the velocity. The coupling of upper- and lower-layer disturbances of such disparate horizontal scales in a single unstable mode is dramatic and unexpected.

Higher modes have successively shorter horizontal scales, though the difference between modes becomes small for long intervals, and show a similar progression toward disparate upper- and lower-layer horizontal scales for shorter intervals. Figure 6(a) shows the lower-layer velocity v_2, at the phase at which it attains its peak northward value, for each of the first three modes. (The peak value has been normalized to unity). The 'quantization' of the modes is evident, as higher modes have successively more relative extrema in a decay length. The corresponding phase-averaged heat fluxes (figure 6b) are similarly quantized. (Note the different structure for the higher modes, with two relative maxima near the exit point.) A given net northward heat flux can thus be expected to require more kinetic energy for successively higher modes, yielding a physical explanation for the successive decrease in growth rates. The heat fluxes for the modes normalized as in figure 6(a) decreases with mode number, as shown in figure 6(b).
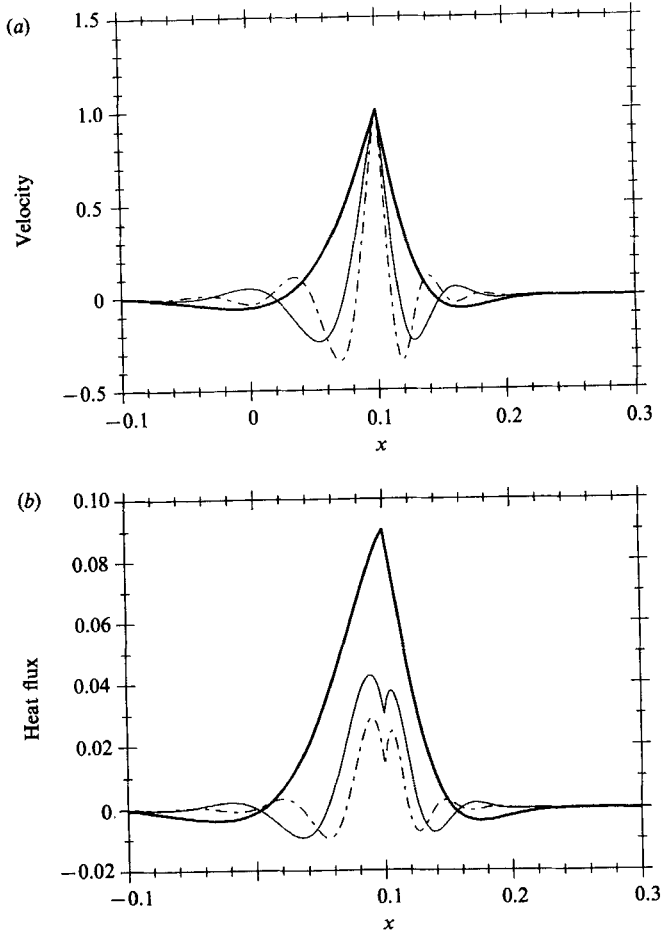
FIGURE 6. (a) v_2 (b) $\frac{1}{2}\text{Re}(\hat{v}_2\,\phi_T^*)$ versus x for $a = 0.1$. ——, Mode 1; ——, mode 2; ---, mode 3.

Further insight into the structure and dynamics of the unstable modes can be gained from approximations to the plane waves (14)–(16) for low frequencies, $|\omega| \ll 1$. The vertical structure of the plane waves is more apparent if layer streamfunctions are considered, with

$$\phi_1 = A_1\,e^{i(kx-\omega t)}, \quad \phi_2 = A_2\,e^{i(kx-\omega t)}, \tag{26}$$

instead of (14). Substitution of (26) into (6) yields the dispersion relation (15) plus the additional long barotropic wave solution $k = 0, A_1 = A_2, \omega$ arbitrary. The amplitudes obey

$$[(\omega - kU)\,(k^2+1) + (\beta+U)k]A_1 - (\omega-kU)A_2 = 0. \tag{27}$$

Along with the $k = 0$ wave, the approximate solutions of (15) and (27) for low frequencies are a long baroclinic wave,

$$k \approx -\frac{\beta+\beta_2}{\beta(\beta_2-U)}\omega, \quad A_2 \approx -\frac{\beta}{\beta_2}A_1, \tag{28}$$

two surface-trapped quasi-stationary resonant waves,

$$k \approx \pm(\beta/U)^{\frac{1}{2}} + \frac{\beta(\beta_2-U)+\beta_2 U}{2\beta U(\beta_2-U)}\omega, \quad A_2 \approx \frac{(U/\beta)^{\frac{1}{2}}}{\beta_2-U}\omega A_1 \tag{29}$$

and a short bottom-trapped wave,

$$k \approx -\frac{\beta_2 - U}{\omega}, \quad A_2 \approx \frac{(\beta_2 - U)^2}{\omega^2} A_1. \tag{30}$$

Substitution of $\beta = 0.25$, $U = 1$, $\alpha_s = 2$ into (28)–(30) indicates that for a growing mode the long baroclinic wave will decay upstream, while the latter three decay downstream. The signatures of these waves are evident in the velocity structure of mode 1 for $a = 0.1$ (figure 4e). Upstream the baroclinic wave dominates. Near the exit point, the short bottom-trapped wave allows a narrow jet in the lower layer. Downstream, the resonant waves decay slowly in the upper layer, while lower-layer fluctuations are minimal. The short bottom-trapped wave, which balances time rate of change of relative vorticity with motion in the ambient potential vorticity gradient, evidently plays a crucial role in maintaining the instability for short unstable intervals. As the interval shortens, the instability weakens and its frequency and growth rate decrease. This shortens the wavelength of the relative vorticity–ambient gradient balance in the lower layer, allowing the instability to occur for successively shorter unstable intervals. As the unstable interval increases in length, the resonant waves (29) begin to propagate and their wavelength decreases, eventually approaching that of the homogeneous unstable waves. The short wave continues to support rapid variations in the lower-layer velocity near the exit point.

The approximations (28)–(30) may be used to formulate a perturbation theory that yields an approximate analytic eigenvalue equation for all modes for small a and $|\omega|$. For this analysis, the matching problem is most conveniently formulated in terms of the layer streamfunctions ϕ_1 and ϕ_2, using the ten matching conditions (18) and (19), and allowing long barotropic ($k = 0$) fluctuations only in the interval and westward, according to (12). (This formulation is equivalent to that using (12), (17) and (20).) The long barotropic ($k = 0$) and baroclinic (28) waves are retained in both layers, both upstream and in the unstable interval, as in the full problem. The surface-trapped waves (29) are retained in the interval and downstream, but only in the upper layer. The bottom-trapped wave (30) is also retained in the interval and downstream, but only in the lower layer. The *a priori* neglect of the lower-layer part of the surface-trapped wave and the upper-layer part of the bottom-trapped wave, motivated by the strong trapping for small $|\omega|$ indicated by (29) and (30), allows considerable algebraic simplification. (The perturbation theory may be motivated more formally by a multiple-scaling procedure, not repeated here.) The solutions satisfy all the boundary and matching conditions, and the resulting determinant is 10×10, but it can be reduced to 4×4 by relatively few Gaussian elimination steps.

The result of the perturbation analysis is the approximate eigenvalue equation,

$$\exp(2ip) = \frac{K^2 p^2}{a^2} + O\left(\frac{a}{\omega}\right), \tag{31a}$$

where

$$p = \frac{(U - \beta_u) a}{\omega}, \tag{31b}$$

$$K = \left| \frac{\beta_s - U}{\beta_s - \beta_u} \right|, \tag{31c}$$

and $\beta_u = \alpha_u + \beta$, $\beta_s = \alpha_s + \beta$. Let
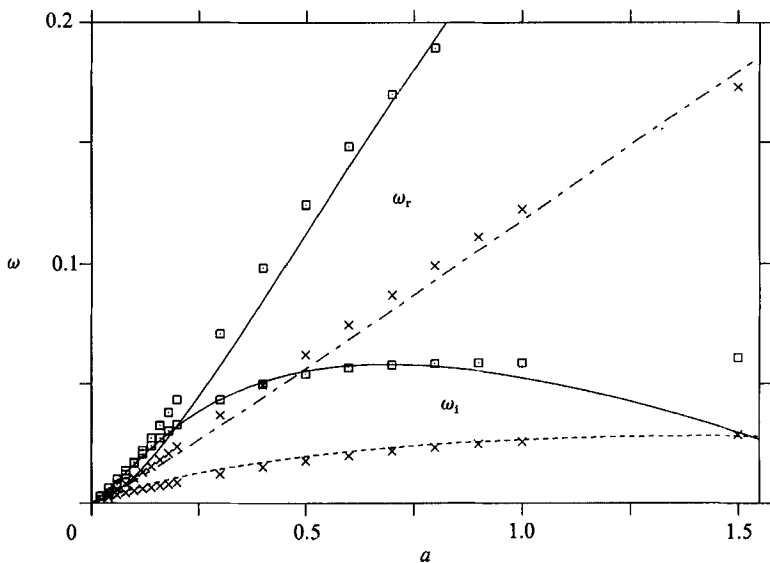
$$p = P e^{-i\chi} \tag{32}$$

FIGURE 7. Frequency ω_r and growth rate ω_i versus interval half-length a. Perturbation result: ——, mode 1; ——— mode 2. Full matching solution: □, mode 1; ×, mode 2.

in (31 a) to obtain the two relations

$$P \sin \chi = \ln \frac{KP}{a}, \qquad (33a)$$

$$P \cos \chi = -\chi. \qquad (33b)$$

These may be used to solve the transcendental equation (31 a) parametrically for ω as a function of a,

$$\omega = (U - \beta_{\mathrm{u}}) K \, \mathrm{e}^{-\chi \tan \chi} \mathrm{e}^{\mathrm{i}\chi}, \qquad (34a)$$

$$a = -K\chi \sec \chi \, \mathrm{e}^{-\chi \tan \chi} \mathrm{e}^{\mathrm{i}\chi}. \qquad (34b)$$

Solutions with $\omega, a \ll 1$ and $\omega_r > 0$ are found near negative half-integer multiples of π, that is, for $\chi = (\frac{1}{2} - m)\pi - \epsilon, \epsilon > 0, m = 1, 2, \ldots$, where m then corresponds to the mode number. Figure 7 shows the eigenvalues versus a for the first two modes from (34) and from the full matching solution. The perturbation theory is remarkably accurate up to $a \approx 1$ for mode 1 and beyond for mode 2. The growth rate prediction is slightly better than the frequency prediction.

As $a \to 0$, solutions of (33 a) obey

$$P = \ln \frac{K}{a} \operatorname{cosec} \chi + O(\ln P \operatorname{cosec} \chi), \qquad (35a)$$

which may be substituted into (33 b) to yield the transcendental equation

$$\chi = -\ln \frac{K}{a} \cot \chi + O(\ln P \operatorname{cosec} \chi). \qquad (35b)$$

This has the approximate solutions

$$\chi_m \approx (\tfrac{1}{2} - m)\pi \left[1 + \left(\ln \frac{K}{a} \right)^{-1} \right] \quad (m = 1, 2, \ldots). \qquad (36a)$$
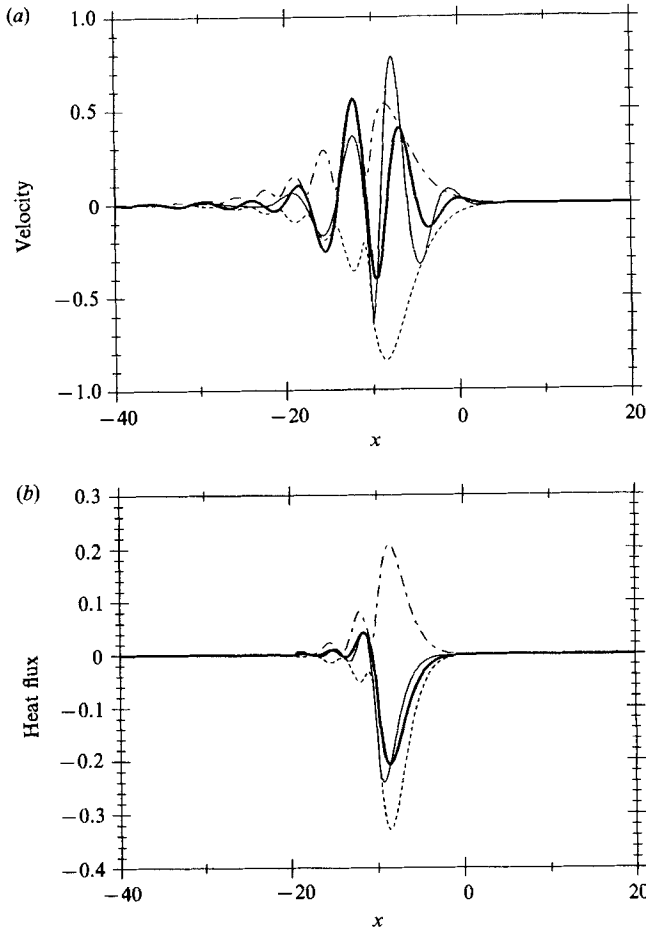
FIGURE 8 (a, b). For caption see page 430.

From $(31b)$, the corresponding approximate eigenvalue relation for mode m is,

$$\omega(\text{mode } m) \approx \left[(m-\tfrac{1}{2})\,\pi + \mathrm{i}\ln\frac{K}{a}\right]\left(\ln\frac{K}{a}\right)^{-2}(U-\beta_{\mathrm{u}})\,a. \tag{36b}$$

For constant a, then, $\qquad \dfrac{\omega_{\mathrm{r}}}{\omega_{\mathrm{i}}}(\text{mode } m) \sim m\dfrac{\omega_{\mathrm{r}}}{\omega_{\mathrm{i}}}(\text{mode } 1). \tag{37a}$

By (30), this means $\qquad \dfrac{k_{\mathrm{r}}}{k_{\mathrm{i}}}(\text{mode } m) \sim m\dfrac{k_{\mathrm{r}}}{k_{\mathrm{i}}}(\text{mode } 1), \tag{37b}$

for the short bottom-trapped wave, so the lower-layer streamfunction for mode m will have roughly m relative extrema near the exit point where the short wave dominates. From (36), ω_{i} is independent of mode number, so that all modes grow at an equal rate in the limit $a \to 0$. For $\ln(K/a) \sim 1$, the approximation (35) rapidly loses accuracy, as the numerical solutions in figure 3 are consistent with the estimate

$$\left|\frac{\omega_{\mathrm{i}}}{a}\right|(\text{mode } m) \sim \left|\frac{\cos\chi}{\chi}\right| \sim \frac{1}{m} \tag{37c}$$

(c)

(d)

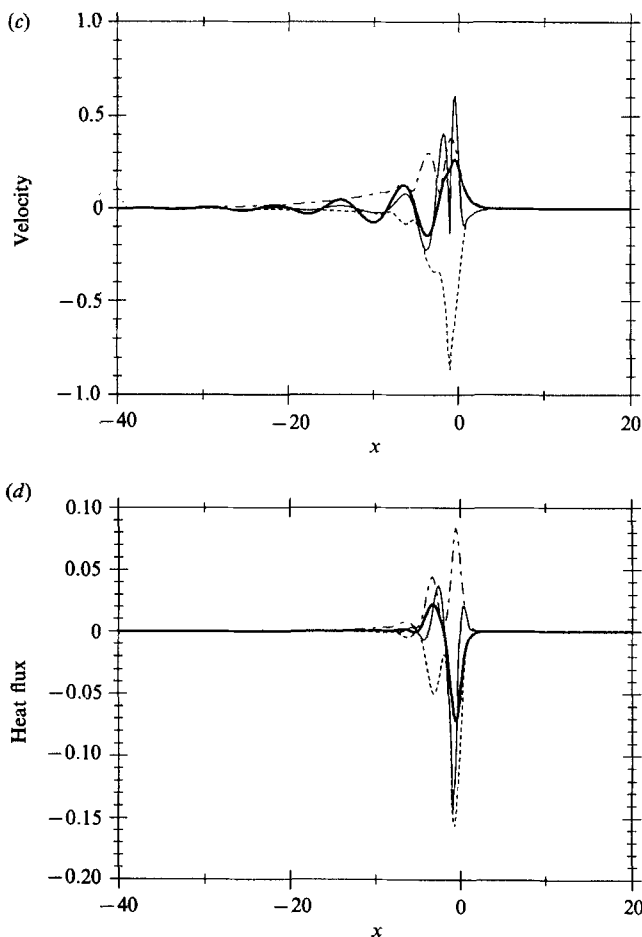FIGURE 8 (c, d). For caption see next page.

obtained from (34) for $|\chi - (\frac{1}{2} - m)\pi| \sim 1$, indicating that growth rates will decrease as $1/m$ for constant a. The results ($37a, b$) evidently hold also for finite a, as they are consistent with the numerical solutions in figure $6(a)$, for which $a = 0.1$.

For $U = -1$ (westward flow), there are no resonant waves, so the modal structure changes qualitatively. Referring to figure 2, we choose $\alpha_u = 0$, $\alpha_s = -2$ for local instability. By (28), the long baroclinic wave still decays toward negative x, but this is now downstream. The 'resonant' wave (29) does not resonate but decays both upstream and downstream, with decay scale $(-\beta/U)^{\frac{1}{2}}$. The short wave again decays downstream. The velocities and heat fluxes for mode 1 with $U = -1$ are shown in figure 8 for the same set of interval lengths as in figure 4, $a = \{10, 1, 0.1\}$. Maximum velocities are greater in the lower layer than the upper even for $a = 10$. The downstream decay is more rapid in the upper layer than for $U = 1$, and less rapid in the lower layer. This difference is due to the decay of the 'resonant' waves (29) for $U = -1$, and the presence of the long baroclinic wave (28) downstream. As a decreases, ω decreases and the downstream decay scale lengthens according to (28). For $a = 0.1$, the velocities and heat fluxes show the same dramatic confinement in the lower layer and diffuse structure in the upper layer as for $U = 1$, with the long baroclinic wave rather than the quasi-stationary resonant waves now determining
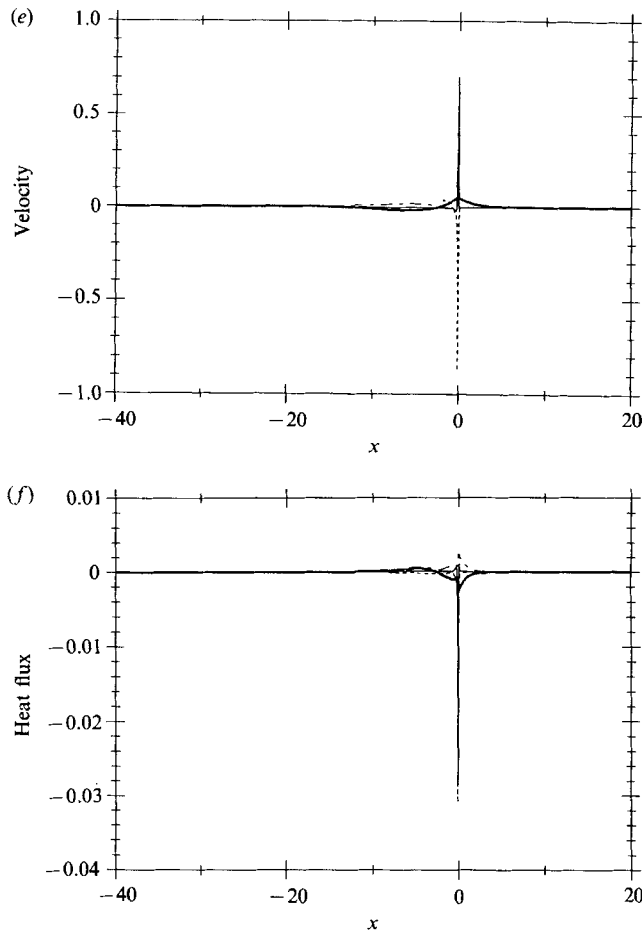
FIGURE 8. As figure 4, but for $U = -1$, $\alpha_u = 0$, $\alpha_s = -2$.

the upper-layer horizontal structure. The dependence of the eigenvalues on a for $U = -1$ (figure 9) is qualitatively very similar to that for $U = 1$, in spite of the difference in mode structure. This suggests that the dynamics of the instability does not depend crucially on qualitative aspects of the downstream decay. The larger growth rates for the case $U = -1$ relative to the case $U = 1$ occur because of the greater local supercriticality (see figure 2).

As Pierrehumbert (1984) and Pedlosky (1989) found, only local maxima in supercriticality are required for the existence of local unstable modes. Growth rates are determined by the maximum supercriticality and do not depend on the degree of stability of the flow exterior to the interval of maximum instability. Eigenvalues for $U = 1$ with exterior slope $\alpha_s = 0.5$ (for which there are unstable waves in the homogeneous problem), and $\alpha_u = 0$ have the same dependence on a as in figure 3. The spatial structure of the modes does change, with weaker trapping for less stable exterior flow.
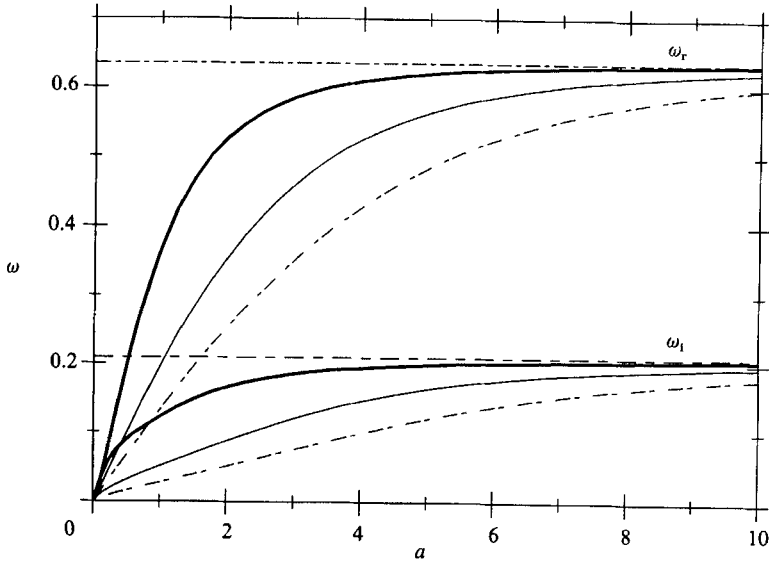
FIGURE 9. As figure 3, but for $U = -1$, $\alpha_u = -0$, $\alpha_s = -2$.

4. Numerical solutions and WKB analysis

For smoothly-varying slope $\alpha(x)$, we have determined the most unstable mode by the timestepping method outlined in §2. The slope is taken to vary exponentially with squared distance,

$$\alpha(x) = 2 - b\,e^{-x^2/2\sigma^2}. \tag{38}$$

We take $U = 1$ and $\sigma = 5\pi$ and vary only b, which controls the maximum local supercriticality of the flow. The domain extends from $x = -20\pi$ to $x = 20\pi$. Global instabilities (Pierrehumbert 1984) are damped by a sponge region, with friction coefficient r increasing to $r = 1$ at its centre, that covers $-20\pi < x < -\frac{1}{3}20\pi$. Elsewhere $r = 0$. The supercriticality is zero for $\alpha = 0.75$ (see figure 2), which occurs for $b = 1.25$. For $b = 2$, the slope vanishes at its minimum at $x = 0$, just as it did in the entire unstable interval in the matching solutions.

Figure 10(a) shows the timestepping solution for the most unstable mode for $b = 2$ at time $t = 450$, when the growth rate and frequency have encouraged. Only the instantaneous layer velocities v_1 and v_2 are shown. These may be compared with the velocities v_1 and v_2 in figure 4(a), for which the minimum value of the slope α is also $a = 0$, as it is for $b = 2$. The timestepping and matching solutions have nearly identical upper-layer velocities. (The phase and amplitude of each solution are arbitrary, so these differences are of no consequence.) The smoothly-varying topography (38) leads to smoother variation of the lower-layer velocity in the timestepping solution. Otherwise, the lower-layer velocities are also very similar, first growing, and then decaying, more rapidly than the upper-layer velocities. The wavelengths of the spatial oscillations agree, and the westward phase shift with height is evident in the region of spatial growth.

It is interesting that if the layer streamfunctions are calculated from the timestepping solutions by (12), the barotropic fluctuations westward 'at infinity' are negligible for the solution shown in figure 10(a). Instead of (38), the topography

$$\alpha(x) = 2 - b\left(\tanh\frac{x+a}{\sigma} - \tanh\frac{x-a}{\sigma}\right)\Big/\left(2\tanh\frac{a}{\sigma}\right) \tag{39}$$
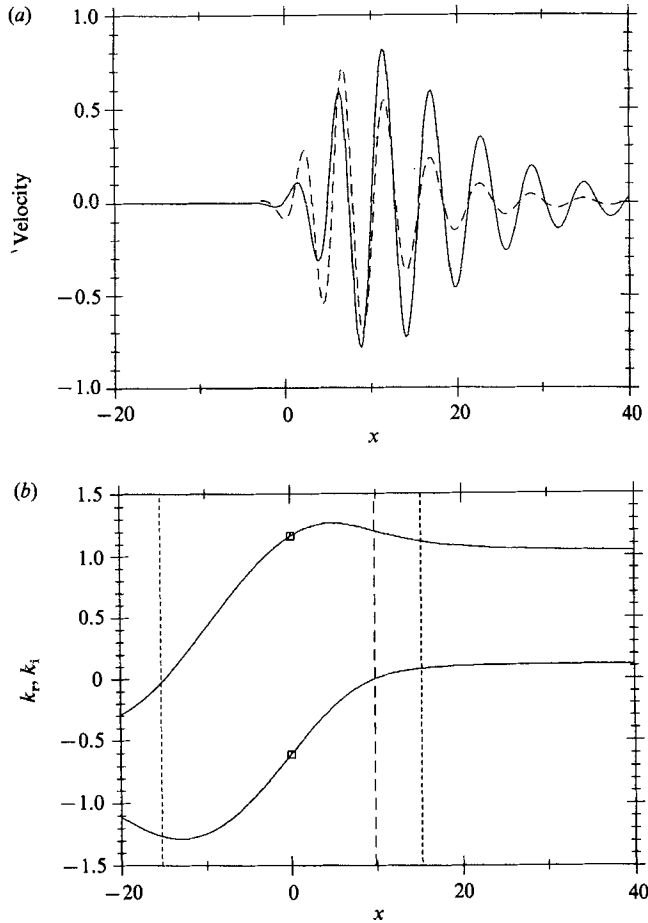
FIGURE 10. (a) Timestepping solution for most unstable mode, $b = 2$, $t = 450$. ———, v_1; ———, v_2 versus x. (b) WKB wavenumber k_r and spatial growth rate k_i versus x. ----, endpoints of interval for absolute instability. ———, location of amplitude maximum.

may be specified, which approaches the abruptly varying case of §3 as $\sigma \to 0$. For $\sigma \lesssim \pi$ (and $a = 10$), timestepping solutions with (39) have appreciable barotropic fluctuations 'at infinity', and approach the fastest-growing mode from the matching problem in increasing detail as $\sigma \to 0$.

Figure 11 shows the growth rates and frequencies for the numerical and matching solutions for $\alpha(0) = \{0, 0.2, 0.4, 0.6\}$ ($b = \{2, 1.8, 1.6, 1.4\}$). For the matching solutions, endpoints of the unstable interval were placed in each case where the topography (38) passes through the critical slope $\alpha = 0.75$. These were at $x(=a) = \{15.2, 13.4, 11.0, 7.5\}$. The agreement is good in both frequency and growth rate.

The WKB results for frequency and growth rate, also shown in figure 11, agree with the numerical and matching solution values. Figures 3 and 9 compare the WKB results with the dispersion relations for ω from the matching solutions. As noted above, the WKB results retain considerable accuracy for intervals of length comparable to the wavelengths of homogeneous unstable waves. For shorter intervals, the WKB results rapidly lose accuracy. For large intervals, the WKB results accurately predict the frequency and growth rate of the most unstable mode
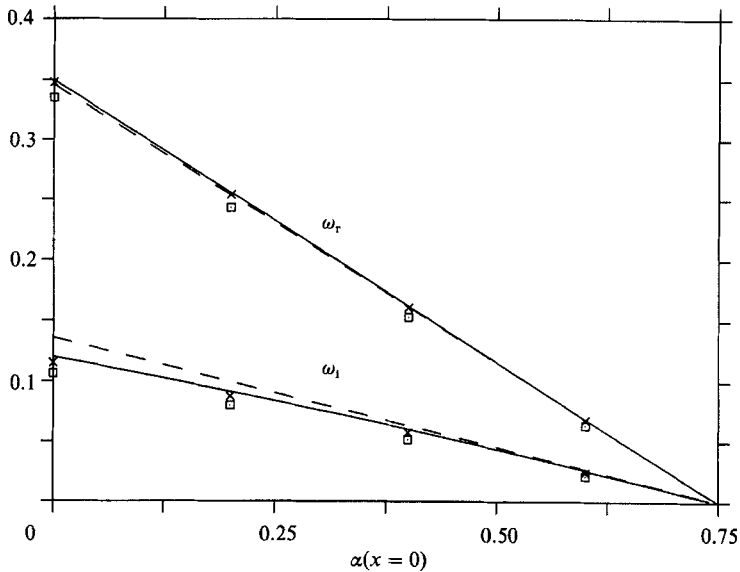
FIGURE 11. Frequency ω_r and growth rate ω_i versus slope at $x = 0$. $\square$, Timestepping; $\times$, matching; ———, WKB result; ———, approximate WKB result.

of the matching problem. Since the matching problem contains abrupt zonal variations in meridional slope, while the WKB results presume only gradual variations, this agreement is perhaps surprising. This suggests (as for the comparison of $U = 1$ and $U = -1$ matching solutions) that the dynamics of the instability does not depend crucially on qualitative aspects of the disturbance field in the decay region.

We refer the reader to Pierrehumbert (1984) for a detailed exposition of the relevant WKB theory in the context of local instability. The fundamental assumption is that departures from zonal homogeneity are small, that is, the topographic slope varies slowly with x. Then solutions may be sought that behave locally as waves over constant slope and so satisfy (15) locally. The WKB theory (which follows from a generalization to complex ω of the well-known stationary phase approximation) is asymptotic for large time, and so treats only the most unstable mode, which will eventually dominate. The WKB requirement for local instability is that $d\omega/dk = 0$ at the point of maximum local supercriticality.

Figure 10(b) shows the local wavenumber of the WKB solution for $b = 2$ ($\alpha(0) = 0$), for which the numerical solution is shown in figure 10(a). The coalescence point at $x = 0$ is indicated. The maximum amplitude of the mode will be attained where the imaginary part of the wavenumber changes sign and the mode begins to decay downstream (shown by the long-dashed line). This corresponds well with the location of maximum amplitude in the numerical solution. For comparison, the endpoints of the unstable interval (where the topographic slope passes through critical) are also shown.

Figure 11 shows the numerical, matching and WKB eigenvalues ω, versus slope at $x = 0$. The supercriticality $\Delta = U - \beta_2 = U - \beta - \alpha = 0.75 - \alpha$ so $\Delta = 0$ when $\alpha = 0.75$. Growth rates increase linearly with supercriticality. This contrasts sharply with the zonally homogeneous problem, in which the growth rate increases as the square root of the supercriticality (Pedlosky 1979). The local instability constraint leads to a

weaker increase of growth rate with small supercriticality. Note that the frequency and growth rate for $\alpha(0) = 0$ agree with the results (his figure 7, $\bar{U} = 0.5$) of Pierrehumbert (1984) for slowly-varying basic flow. The WKB results must agree, since they depend only on the flow parameters at the location of maximum supercriticality, which are identical when $\alpha(0) = 0$.

For $\varDelta \ll 1$ this linear dependence of growth rate on supercriticality may be analytically approximated from the WKB theory. In (15) let $\omega = \Omega\varDelta + O(\varDelta^2)$. Then

$$\Omega = \frac{(\beta - Uk^2)\,k}{-Uk^2(k^2+2)+(\beta+U)\,(k^2+1)}.$$ (40)

The local instability condition $\mathrm{d}\Omega/\mathrm{d}k = 0$ then yields

$$U^2k^6 - U(2\beta+U)\,k^4 + (\beta^2 + 2\beta U + 3U^2)\,k^2 + \beta(\beta+U) = 0,$$ (41)

which may be solved for k given β and U. The result (for the unstable mode with $\mathrm{Im}\,\Omega > 0$) is shown as the dashed line in figure 11 for $U = 1$, $\beta = 0.25$. The agreement even for large supercriticality is remarkable. For general β and U, the accuracy of (40) and (41) is only guaranteed for $\varDelta \ll 1$.

5. Dimensional quantities and frictional effects

Although the model problem studied here is idealized, it is of interest to make some rough estimates of dimensional parameters based on atmospheric and oceanic scales.

The basic scales are U_* (the basic state velocity scale) and L_R (the internal deformation radius). Typical deformation radii are $L_R = 1000$ km for the atmosphere and $L_R = 50$ km for the ocean. For corresponding velocity scales $U_* = 80$ m s^{-1} and $U_* = 20$ cm s^{-1}, respectively, and mid-latitude variation of Coriolis parameter with latitude $\beta_* = 2 \times 10^{-11}$ m^{-1} s^{-1}, these yield a non-dimensional $\beta = 0.25$, as above, and timescales $T = L_R/U_*$ of 3.5 h and 3 days, respectively. The growth rates for the eastward flow of figure 3 and an unstable interval of length L_R ($a = 0.5$) correspond to e-folding times of 2.4 days and 50 days, respectively. These are comparable to observed atmospheric and oceanic timescales for cyclogenesis. More rapid growth rates obtain for stronger shears. Thus, supercritical regions of even quite limited zonal extent support substantial local instabilities.

The main effect of small friction on the above results is to decrease the growth rates by an amount nearly equal to the frictional decay rate. Thus, inviscid modes with growth rates below a given frictional decay rate will decay rather than grow when that friction is imposed. As a result, in the presence of friction the anticipated successive loss of unstable modes with decreasing unstable interval length occurs, while it does not in the inviscid case. For $U = 1$ and $a = 0.5$ as above, setting $r = 0.02$ (dimensional decay times of 7.3 days and 150 days, respectively) increases the e-folding times to 3.6 days and 75 days, respectively.

6. Summary

Local baroclinic instability is studied following an approach, proposed by Pedlosky (1989), that allows the interval of instability (local supercriticality) to be arbitrarily short, circumventing the limitations of conventional WKB analysis. Variable meridional bottom slope controls the supercriticality of a uniform zonal flow in a two-layer quasi-geostrophic model. Solutions are found by matching

pressure, velocity, and upper-layer vorticity across points where the bottom slope changes abruptly so as to destabilize the flow in a central interval.

Remarkably, an infinite number of unstable modes exists for arbitrarily short intervals. This contrasts with the heuristic models of Pedlosky (1989), in which successive modes are lost as the interval shortens. The growth rates for these modes decreases as $1/m$ with mode number m for short intervals, but are independent of m as the interval length approaches zero. We speculate that this infinity of modes, associated with the singular behaviour of (31) as $\omega \to 0$, depends upon the absence of mean flow advection in the lower layer relative to the supercritical interval. Hence we are reluctant to generalize this aspect of our result to more general flow. The addition of small friction introduces a growth-rate threshold and results in successive loss of modes with decreasing interval length, as in the heuristic model.

WKB results for growth rate and frequency for the most unstable mode in flow over slowly varying slope are accurate for long intervals but lose accuracy for intervals of length comparable to and smaller than the wavelengths of unstable waves in the homogeneous problem. The matching solution local modes retain large growth rates (about half maximum) for intervals as short as the internal deformation radius, and considerably shorter than the wavelengths of the shortest homogeneous instabilities. For intervals shorter than the deformation radius, growth rates decrease rapidly. Evidently, the deformation radius and not the homogeneous instability determines the fundamental horizontal scale for local instability.

The modes are weakly trapped in the upper layer, yielding resonant Rossby waves in eastward flow and long baroclinic waves in westward flow for short intervals and small growth rates, while the lower-layer amplitudes decay more rapidly. Heat flux is more strictly confined to the supercritical interval than amplitude. The coupling of disparate horizontal lengthscales in the upper and lower layers in a single unstable mode for short intervals is dramatic and unexpected. Only local maxima in supercriticality are required for the existence of local unstable modes, in agreement with previous results (Pierrehumbert 1984; Pedlosky 1989). For all interval lengths, maximum mode amplitudes occur near the downstream edge of the interval. Growth rates increase linearly with supercriticality for weakly supercritical flow, in contrast to the more rapid square-root of supercriticality growth in the homogeneous problem.

The present work treats linear instabilities without meridional variation. A natural question concerns the effect of meridional confinement on the linear modes. This problem is under investigation. It is also tempting to speculate that the nonlinear equilibration of local instability processes similar to these may be associated with the genesis of blocking patterns and coherent vortex structures, though the physical structure of the local modes for short intervals is more complex than the simple 'bound eddy' mode of the heuristic models of Pedlosky (1989). A quasi-stationary Rossby wave forms in the upper layer, growing in time and decaying downstream, while a narrow jet in the lower layer grows and fluctuates in phase with the upper layer flow.

REFERENCES

CHARNEY, J. G. 1947 The dynamics of long waves in a baroclinic westerly current. *J. Met.* **4**, 135–162.

EADY, E. T. 1949 Long waves and cyclone waves. *Tellus* **1**, 33–52.

FREDERIKSEN, J. S. 1983 Disturbances and eddy fluxes in northern hemisphere flows: Instability of three dimensional January and July flows. *J. Atmos. Sci.* **40**, 836–855.

GENT, P. R. & LEACH, H. 1976 Baroclinic instability in an eccentric annulus. *J. Fluid Mech.* **77**, 769–788.

HOLOPAINEN, E. O. 1983 Transient eddies in mid-latitudes: Observations and interpretation. In *Large-Scale Dynamical Processes in the Atmosphere* (ed. B. Hoskins & R. Pearce), chap. 8. Academic.

MERKINE, L. & SHAFRANEK, M. 1980 The spatial and temporal evolution of localized unstable baroclinic disturbances. *Geophys. Astrophys. Fluid Dyn.* **16**, 174–206.

PEDLOSKY, J. 1979 *Geophy. Fluid Dyn.* Springer, 624 pp.

PEDLOSKY, J. 1989 Simple models for local instabilities in zonally inhomogeneous flows. *J. Atmos. Sci.* **46**, 1769–1778.

PHILLIPS, N. A. 1954 Energy transformations and meridional circulations associated with simple baroclinic waves in a two-level quasi-geostrophic model. *Tellus* **6**, 273–286.

PIERREHUMBERT, R. 1984 Local and global baroclinic instability of zonally varying flow. *J. Atmos. Sci.* **41**, 2141–2162.